

# Acceleration of Fully 3D Monte Carlo Based System Matrix Computation for Image Reconstruction in Small Animal SPECT

Ziad El Bitar, Virgile Bekaert, and David Brasse

**Abstract**—It has already been proved that Fully Three Dimensional Monte Carlo (F3DMC) is a robust image reconstruction algorithm that can be applied in Single Photon Emission Computed Tomography (SPECT) and small animal Positron Emission Tomography (PET). F3DMC has still not yet been validated on real data in small animal SPECT application. The advantage of such image reconstruction technique is that all the physical processes occurring within the detector and its geometrical parameters can be precisely modelled within the system matrix thanks to powerful Monte Carlo Simulation toolkit. Once the system matrix is computed, it can be integrated within an iterative reconstruction algorithm such as Maximum Likelihood Estimation Maximization (MLEM) in order to resolve the inverse image reconstruction problem. However, such reconstruction technique is penalized by the huge time consumption required for the computation of the system matrix since the accuracy of this latter requires the simulation of large number of photons tracks from the imaged subject to the detector. In this study, we proposed two main solutions to tackle the problem of time consumption. The first has already been proposed in anterior works and consists in parallelizing the Monte Carlo simulations performed with the Geant4 toolkit on a Computing Grid (CG) and the second suggests to apply a Forced Detection (FD) technique in order to accelerate the convergence of the system matrix elements. Results show that an accelerated version of a F3DMC technique is feasible in a reasonable delay and leads to reconstructed images with good spatial resolution and a good capability of restoring relative quantification. Hence, it has been proven that F3DMC is an applicable reconstruction technique in small animal SPECT.

**Index Terms**—Image reconstruction, Monte Carlo methods, single photon emission computed tomography.

## I. INTRODUCTION

**F**ULLY THREE DIMENSIONAL MONTE CARLO (F3DMC) image reconstruction technique has proven its efficiency when applied in clinical Single Photon Emission Computed Tomography (SPECT) [1], [2], small animal SPECT [3], Positron Emission Tomography (PET) [4] and in small animal PET [5], [6]. In the case of preclinical SPECT, studies were performed only on simulated data and for the correction of attenuation and scatter. The considered technique has not

yet been validated using real data in small animal SPECT. In SPECT as well as in PET, the main idea of the F3DMC technique is the use of Monte Carlo Simulations (MCS) to compute the system matrix to be integrated within an iterative reconstruction algorithm such as MLEM [7]. As the robustness of the system matrix is highly correlated to the number of photons tracks [8], the main drawback of the F3DMC technique remains the huge time consumption required to obtain a noiseless system matrix. In order to increase the efficiency of MCS, variance reduction technique (VRT) known as Forced Detection (FD) was proposed by [9]–[11] and [12]. Using the FD technique, each emitted photon is forced towards the collimator holes. This technique leads to an important increase in the number of detected photons. Another acceleration technique using a kernel-based forced detection (KFD) was proposed by [13] for small animal SPECT, and by [14] and [15] for clinical SPECT. It consists in projecting a pre-calculated analytical point spread functions (PSFs) on the detector surface. The speed-up factor can easily reach 3 orders of magnitude when using the KFD technique instead of the FD technique. Only attenuation within the collimator which was analytically defined was considered within the pre-calculated PSFs in small animal SPECT [13]. This means that the implemented KFD technique did not take into account for the interactions processes that occur within the collimator material and the crystal. In order to accurately simulate the PSFs, one needs to simulate the interactions occurring within the detector crystal and the collimator [16]. Most often, the speed up factor is computed without taking into account the time required for the calculation of the PSFs when analytical methods are used [13]. In this work, we first compared the calculation of the PSFs integrating the interactions within the crystal using two methods: in the first one, the collimator response was analytically modelled while in the second one the response of the collimator was modelled using Monte Carlo simulations. In both methods, trajectories of photons that cross the collimator are modelled in the crystal using Monte Carlo simulations. Within this paper, the first method will continue to be referred as the KFD method and the second one as the FD method. Comparison for both methods are made in terms of time computation and memory space requirement for the storage of the PSFs tables. Both methods represent similar computing time in order to model projections with approximately the same noise level. In addition, PSFs tables computed with the FD method require less memory space. For this latter reason, FD technique will be used for all reconstructions in this paper.

Manuscript received May 28, 2010; revised September 09, 2010 and October 26, 2010; accepted November 21, 2010. Date of publication January 10, 2011; date of current version February 09, 2011.

The authors are with the Institut Pluridisciplinaire Hubert Curien, UMR 7178—CNRS/IN2P3 and UDS, BP 28-23, 67037 Strasbourg Cedex 02, France (e-mail: ziad.elbitar@ires.in2p3.fr).

Color versions of one or more of the figures in this paper are available online at <http://ieeexplore.ieee.org>.

Digital Object Identifier 10.1109/TNS.2010.2096292

In the last decades the availability of huge computing power such as Computing Grid (CG) architecture and the feasibility of parallel MCS thanks to independent random number sequences [17], [18] encourage us to revisit the (FD) technique integrating it within parallel MCS in order to compute the system matrix in small animal SPECT. In this work, we present a large scale deployment of MCS on CG architecture available in our institute in order to compute the system matrix corresponding to a small animal SPECT developed by our group [19]. The used CG architecture is a part of the worldwide Large Hadron Collider (LHC) computing grid (<http://lcg.web.cern.ch/LCG>). The LHC is the world's largest and highest-energy particle accelerator. The efficiency of MCS is improved by using the FD detection technique. Reconstructed images of realistic projections acquired from a Derenzo phantom shows that accelerated image reconstruction technique leads to images with a good spatial resolution. Preclinical studies on mice have also demonstrated the realistic feasibility of an Accelerated F3DMC (AF3DMC) reconstruction technique.

## II. MATERIALS AND METHODS

### A. Concept

In small animal SPECT, image reconstruction is an inverse problem that can be represented in a discrete form as:

$$R \times f = p. \quad (1)$$

Where  $R$  is the system matrix that projects the image into the detector,  $f$  is the radioactivity distribution function within the imaged patient/object and  $p$  are the projections of the image on the detector.  $R$ ,  $f$  and  $p$  have respectively the following dimensions:  $(P \times M \times N, V^3)$ ,  $V^3$  and  $P \times M \times N$ .  $P$  represents the number of projections,  $M \times N$  represents the number of detector bins within each projection and  $V^3$  is the number of voxels of the sampled image within the detector Field Of View (FOV). Each element  $R(i,j)$  of the system matrix represents the probability that a photon emitted in voxel  $j$  is detected within the  $i$ th detector bin. In the F3DMC approach, elements of the system matrix  $R$  are computed thanks to MCS. MCS enable photon tracking from its emission point till the detector taking into account all the physical processes occurring within the imaged object and/or the detector as well as all the geometrical parameters.

### B. System Description and Performances

The small animal SPECT system on which the study was applied is composed of four detection heads [19]. Fig. 1 shows a drawing of a detection head. Each detection head comprises five separated detection modules arranged along an arch of a 58 mm radius circle and pointing to the pinhole collimator. A detection module is composed of a YAP:Ce matrix of  $8 \times 8$  scintillating crystals,  $2.3 \times 2.3 \times 28$  mm<sup>3</sup> each, coupled to a multi-anode photomultiplier ( $8 \times 8$ ) (Hamamatsu H8804) matching the size of the matrix with anode pitch of 2.3 mm and an active area of  $2 \times 2$  mm<sup>2</sup>. The collimator is made of tungsten, has a keel-edge shape and a 0.5 mm diameter hole. The distance from the collimator to the axis of rotation of the SPECT is 28 mm and the

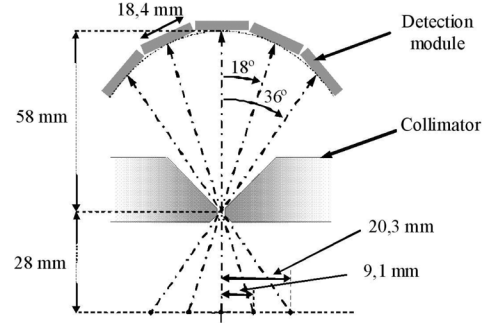


Fig. 1. Drawing of a detection head.

distance from the collimator to the crystal is 58 mm which results in a magnification factor of 2.07. The energy resolution of the system is  $32\% \pm 2\%$  using  $^{99m}\text{Tc}$  (140 keV) as radioactive source. Extrinsic system sensitivity was measured and found to be 84 cps/MBq. As the crystal is pixellized, spatial resolution of the system in planar mode was assumed to be equal to the width of a crystal's pixel which is 2.3 mm.

### C. The Forced Detection

In order to improve the efficiency of MCS, [10]–[12] have proposed to use a VRT based on a FD technique. As in pinhole collimation, few number of photons manage to cross the collimator, it is unnecessary to emit photons in  $4\pi$  since only photons that arrive around the centre of the pinhole have a chance to cross the collimator. It was hence proposed to force the direction of emitted photons towards a circular area centered at the pinhole in order to reduce the number of lost photons. The surface of the area was chosen so that photons with detection probability as low as  $10^{-3}$  are still simulated. Indeed, when using the FD technique, the number of detected photons have to be weighted in order to compensate the fact that emission was constrained within a limited solid angle and not in  $4\pi$ . The applied weight on each detection bin take as parameters the position  $S$  of the emission point, the position  $P$  of the intersection between the photon trajectory and the circular area and of the angle  $\phi$  between the photon direction and the vector normal to the circular area (cf. Fig. 2). The Weight Factor (WF) can hence be written as follows:

$$WF = \frac{\cos \phi}{|S - P|^2}, \quad (2)$$

### D. The Kernel Based Forced Detection

The analytic method describing the photon absorption within the collimator is clearly described in [13], [20] and [21]. Is is based on an analytic calculation of the photon's path length through the collimator given its emission and its detection points. In the previous works, only a single ray was traced from a certain voxel to a detector pixel. To better mimic a realistic photon emission during this work, the implementation of the KFD method differed from previous implementations in the fact that many rays were traced from a certain voxel to

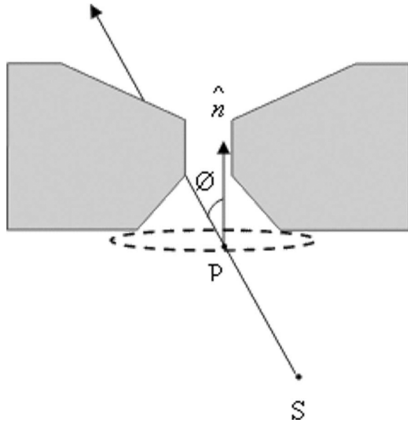


Fig. 2. Geometry of a pinhole collimator. A photon is emitted at a point S and cross the circular area placed at the entry of the pinhole aperture at a point P.  $\phi$  is the angle between the direction of the emitted photon and the normal vector of the circular area.

a detector pixel and that photons' directions were randomly selected towards the same circular used for the FD technique.

#### E. MCS and System Matrix Computing Parallelization

Parallel MCS using the Geant4 toolkit [22] were performed on the available CG in our institute. Physical processes like photoelectric absorption, Compton scattering and Rayleigh scattering were all activated within simulations. Tungsten characteristics x-rays were not included since their energy (70 keV) are not in the photopeak window of 140 keV  $\pm 32\%$ . A continuous source distribution was simulated over the FOV so that the data are processed post-simulation to determine the origin of the gamma ray as well as the positions of interactions. No attenuation medium was introduced within the FOV.

In recent works, [17], [18] have proved the big interest of parallelizing MCS on a CG architecture. The speed-up in computing time depends on the number of available Computing Elements (CE). A CE is a Central Process Unit (CPU) available on a CG. Thanks to a technique called "sequence splitting" which consists in splitting a Random Number Generator (RNG) cycle into non-overlapping contiguous sections, it is possible to store parameters initializing a RNG in order to have independant random number sequences. These latter parameters are stored in files called statuses files. Using these statuses files, parallel MCS with as less correlation as possible can be performed. We have chosen the Mersenne Twister (MT) [23] RNG due to its large period which is  $2^{19937}$ . The CG is composed of 128 bi quad-core Xeon L5420. In Fig. 3, we present a scheme describing the different steps of a parallel computing task going from the computing job submission till the retrieval of the output file. We remind that the management of a job in the grid environment is made through a User Interface (UI) machine. Hereby are the different steps of a job on a computing grid.

- All the files required for the simulations should be stored on the UI machine. These files include the statuses files, the binary of the geant4 simulation and all the other binaries required for the treatment of the simulation output data.
- A Job Description Language (JDL) file corresponding to each computing job has to be defined. A JDL file is a file

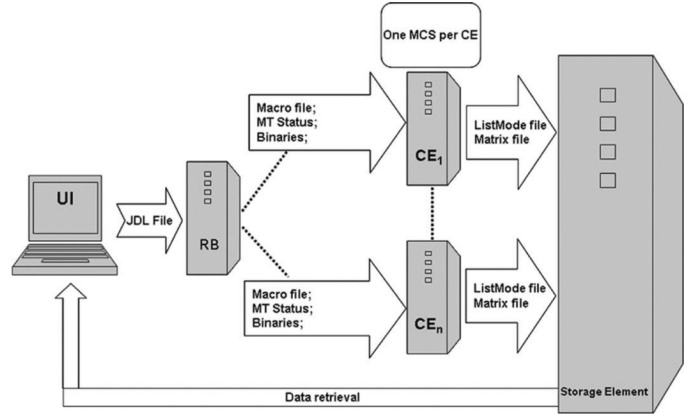


Fig. 3. Submission of parallel jobs on the Grid. As input, each CE takes different random number sequences. Each CE performs an independant MCS, generates a raw data file, computes a list mode data file from the raw data file and finally generates the system matrix corresponding to an elementary list mode data file.

listing all the files and the requirements of the computing job. The JDL file is then sent to the Resource Broker (RB) machine who looks up for CEs whom configuration satisfies the requirement of the computing job.

- The RB machine attributes the computing job to a CE where all the calculations are performed. The different computation tasks performed by each CE are the followings:
  - 1) Execute an independant Geant4 simulation.
  - 2) Create a List Mode file from the output of the simulation.
  - 3) Create a system matrix from the previously created List Mode file. System matrices created on different CEs are called elementary matrices.
- When the computing jobs are finished on all the CEs, the output files are sent to a Storage Element (SE) architecture. Finally we can retrieve the raw data from the SE into the UI machine

Doing so has the advantage of reducing the memory size required for the storage of all the raw data since elementary system matrix is sparse. Another advantage is to reduce the time required to retrieve the raw data. Specific treatment is applied on elementary system matrices in order to merge them into one single system matrix that will be used for the iterative reconstruction. For more information about grid computing, we recommend to visit the following website (<http://glite.web.cern.ch/glite/>).

#### F. Validation Methods

We implemented the FD technique within the Geant4 Monte Carlo simulation toolkit. The accuracy of the FD implementation was validated by comparing it with MCS where photons are emitted isotropically in  $4\pi$ . For this purpose, we simulated a cylinder of  $^{99m}\text{Tc}$  having a diameter of 30 mm and a height of 4 mm. When the forced detection technique was applied, the simulations were performed on a single PC (Intel (R) Core(TM)2 Quad CPU 2.83 GHz). When isotropic emission was performed within the MCS, these latter were parallelized on

the CG due to the large number of photons required to get projections with noise level comparable to those obtained when FD technique was used. Projections obtained with the FD technique were compared to those obtained when isotropic emission was applied. We also compared images of the considered cylinder obtained from the pre-mentioned projections.

### G. Comparison Between FD and KFD

In order to compare between FD technique and KFD technique, we simulate the projections of a point source containing  $^{99\text{m}}\text{Tc}$  located at the center of the field of view. We first calculate the projections of the considered point source obtained by the KFD technique at the entrance of the crystal. These latter projections included only the attenuation in the collimator but not the interactions occurring within the crystal. The projections of the point source were then calculated using the KFD and the FD methods with taking into account for the interactions occurring within the crystal. Projection calculations were made for different numbers of emitted photons:  $10^4$ ,  $10^5$  and  $10^6$ . Furthermore, we compute for each set of projections the Normalized Mean Square Errors (NMSE) in the estimated projections using a reference projection:

$$\text{NMSE} = \sum_i (e_i - r_i)^2 \quad (3)$$

where  $e_i$  represents the normalized pixel values of the estimated projections and  $r_i$  represents the normalized pixel values of the reference projection. All the bins of the projection are considered in the computation of the NMSE. The reference projection is a high count FD projection where  $10^8$  photons are simulated.

### H. Projections Clustering

During this work, the dimensions of the Field Of View (FOV) were fixed to  $10 \times 42 \times 42 \text{ mm}^3$  within the simulations. Two sampling cases were considered, the first is when the FOV was sampled into  $20 \times 84 \times 84$  voxels and the second is when it was sampled into  $30 \times 126 \times 126$  voxels. Hence, voxel dimensions were respectively  $0.5 \times 0.5 \times 0.5 \text{ mm}^3$  and  $0.33 \times 0.33 \times 0.33 \text{ mm}^3$ . For 128 acquired projections, each sampled to  $8 \times 40$  pixels, the system matrix dimension will be  $(20 \times 84 \times 84, 128 \times 8 \times 40)$  or  $(30 \times 126 \times 126, 128 \times 8 \times 40)$  and the required memory sizes for storage in simple precision are respectively 23.1 GB or 78 GB whose management are unfeasible on an actual single standard processor. To address this problem, we have proceeded to the storage of a sparse system matrix. The sparse system matrix stores only the non-zero elements of the full matrix. Furthermore, for each voxel, we define a cluster of pixels of interest (POI) within the detector. The centre of a POI's cluster relative to each voxel is geometrically defined as the intersection point of the line joining the emission voxel and the centre of the collimator with the detector plan. A POI cluster is composed of the central pixel and a predefined number of neighbouring pixels. The impact of the number of the pixels within a POI's cluster was studied and 3 cases were considered corresponding to POI clusters composed of respectively 9 pixels (central pixel + 8 neighbouring pixels), 25 pixels (central pixel + 24 neighbouring pixels) and finally

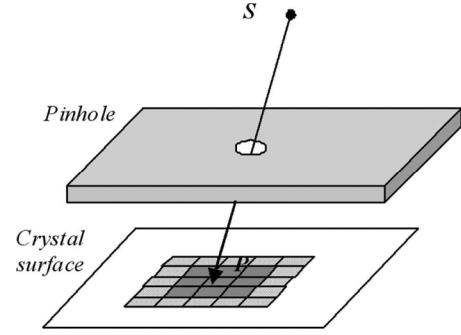


Fig. 4. Projections clustering. Dark grey : 9 POI, light grey : 25 POI.

to the case where no POI clusters are defined and hence all the pixels are considered (cf. Fig. 4). Even when POI strategy is adopted, only non zero elements of the system matrix were stored. In the remainder of this paper, matrix computed by taking into account 9 POI, 25 POI and all the pixels within the projections will be respectively referenced as  $\text{matrix}_9$ ,  $\text{matrix}_{25}$  and  $\text{matrix}_{\text{all}}$ .

### I. Influence of the Number of Photons Tracks Used for the System Matrix Calculation on the Reconstructed Images

The impact of the number of photons tracks used for the system matrix calculation was studied by reconstructing images of the uniform cylinder (diameter = 30 mm, height = 4 mm) using matrices obtained with different number of photons tracks. This study required the obtention of noiseless projections. Thanks to the symmetry revolution of the cylinder, noiseless projections were obtained by computing the mean projection of the 128 projections and duplicating it into 128 projections. The figure of merit used was a Signal to Noise Ratio (SNR) defined as the ratio of the mean number of counts within a region of interest (ROI) corresponding to a 20 mm diameter cylinder with a height of 3 mm over its associated standard deviation. The ROI was placed in the center of the reconstructed images.

### J. Quantitative Evaluation

The quantitative evaluation of the AF3DMC algorithm was studied using both simulated and real data. The simulated data consisted of the projections of a Jaszczak phantom type. The Jaszczak phantom type is a 5 mm height and 30 mm diameter cylinder (cf. Fig. 5). Six cylindrical rods are inserted within the considered phantom having respectively the following diameters: 1 mm, 1.5 mm, 2 mm, 2.5 mm and 3 mm for the both largest rods. No activity was inserted within the last rod (rod (6) in Fig. 5) which was considered as the cold rod of the phantom. A background  $^{99\text{m}}\text{Tc}$  activity of 0.31 MBq/ml ( $C_{\text{background}}$ ) was set within the rest of the cylindrical phantom, except within the first five rods, which contained a  $^{99\text{m}}\text{Tc}$  activity equal to five times that of the background ( $C_{\text{hot}} = 1.55 \text{ MBq/ml}$ ). The simulations were performed with the Gate simulation toolkit [24]. A total number of 1000 simulations were parallelized on the CG. The total duration of this simulations was about 3600 hours. Thanks to the grid, these simulations had been performed in 6 hours. Within each simulations, 128 projections, each having a

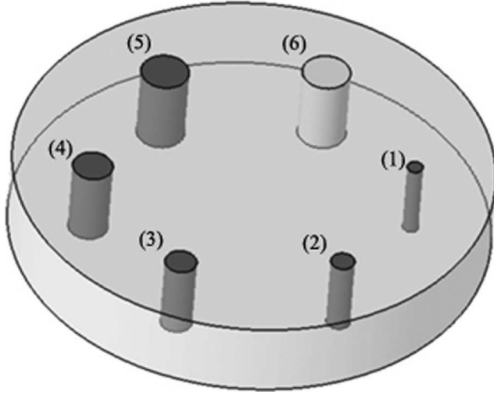


Fig. 5. The Jaszczak type phantom used in the Gate simulations.

duration of 1s were calculated and the energy resolution of the system was fixed to 32 % at 140 keV.

The Restored Activity Ratios (RAR) was chosen as a figure of merit and was computed on the reconstructed images. For each rod, the RAR corresponds to the ratio of the activity concentration measured in the considered rod over the activity concentration measured in the background. For the hot rods and the cold rod, the ROIs had the same dimensions as the rods. The concentration activity in the background was measured within a cylindrical ROI having a diameter of 20 mm and a height of 4 mm. In order to compute the error on the RAR values, we generate 50 replications of the original simulated projections by adding a Poisson noise. The mean number of counts and associated standard deviations were  $33190395 \pm 10399$ . The 50 replicated noisy projections were reconstructed and a RAR value was computed for each ROI on all the reconstructed images. Mean values and standard deviation values were then computed for each ROI over the 50 reconstructed images. Two sets of reconstructed images were done, the first using matrix calculated with  $10^9$  emitted photons per projection and the second with the matrix calculated with  $10^{10}$  emitted photons per projection.

For the real data validation, we used a phantom composed of 13 cylindrical rods disposed as shown in Fig. 6. The used phantom was fabricated in our laboratory. The geometrical parameters and the positions of the rods' centers are very well known. The Restored Activity Ratios (RAR) were computed between a rod placed at the inner ring (grey filled rods) and the central rod, and between a rod placed at the outer ring and the central rod. Each cylindrical rod has an inner diameter of 2 mm and a height of 7 mm and was filled with an activity concentration of 455 kBq/ml of  $^{99m}\text{Tc}$ . The ideal RAR should than be equal to 1. 128 projections over  $360^\circ$ , each of 15 seconds duration were acquired. For activity ratios computation, measurements were done within cylindrical Regions Of Interests (ROI) having a diameter of 2 mm and a height of 5 mm in order to avoid the edge effects. Regions of interest were drawn in the center of the rods within the reconstructed images.

#### K. Tomographic Performances Assessment of the AF3DMC

In order to assess the tomographic performances of the AF3DMC image reconstruction technique, a Derenzo phantom fabricated in our institute was used. The considered Derenzo

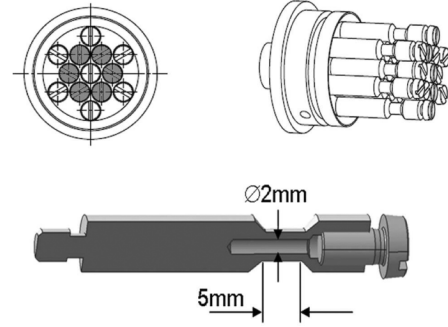


Fig. 6. Phantom used for the relative quantification evaluation of the AF3DMC algorithm. Rods placed on the inner ring are filled with grey.

phantom is a 3 cm inner diameter cylinder including six equally sized rods quadrants. The rods within the quadrants have respectively the following diameters 0.8, 1.0, 1.2, 1.4, 1.6 and 1.8 mm. The phantom was filled with a 166 MBq solution of  $^{99m}\text{Tc}$ . A set of 128 acquisitions was performed over 360 degrees with an acquisition time of 15 seconds per acquisition. Projections are sampled into  $8 \times 40$  pixels of  $2.3 \times 2.3 \text{ mm}^2$  each.

#### L. Preclinical Studies

A volume of 40  $\mu\text{l}$  of pertechnetate  $^{99m}\text{TcO}_4^-$  having an activity of 37 MBq was intraperitoneally injected. The mouse was euthanized one hour after the injection to enable the evaluation of the considered reconstruction technique independently of respiratory motion artifacts. A CT exam was performed enabling the obtention of the mouse attenuation map with a resolution of  $100 \times 100 \times 100 \mu\text{m}^3$ . The images obtained from the CT modality were fused later with those obtained from the SPECT modality for the localization of hot activity regions with respect to the anatomical map. We proceeded then to a SPECT exam, acquiring 128 projections each of 10 s. In order to image the whole body, the SPECT exam was performed for 14 positions of the animal. The step between positions was fixed to 8 mm with an overlap of 2 mm (6 voxels of 0.33 mm). Acquired projections for each position was then reconstructed leading to whole body reconstructed images. Slices corresponding to overlaps were not considered for the whole body images. This strategy was adopted in order to avoid the edge effect artifacts.

### III. RESULTS

#### A. Forced Detection Technique Validation

In order to compute the projections for the 30 mm diameter and 4 mm height cylinder,  $9 \times 10^{11}$  photons tracks were used and  $1.376 \times 10^7$  photons were detected per projection when isotropic emission was considered which yields to a simulated system efficiency of  $1.53 \times 10^{-5}$ . When the FD technique was applied,  $5 \times 10^8$  photons tracks were used and  $3.389 \times 10^6$  photons were detected per projection and simulated system efficiency was then equal to  $6.78 \times 10^{-3}$ . Fig. 7 shows the profile drawn on the central slice of projections computed when FD technique was used and when isotropic emission was applied. Fig. 8 shows the profiles drawn in the center axial slice

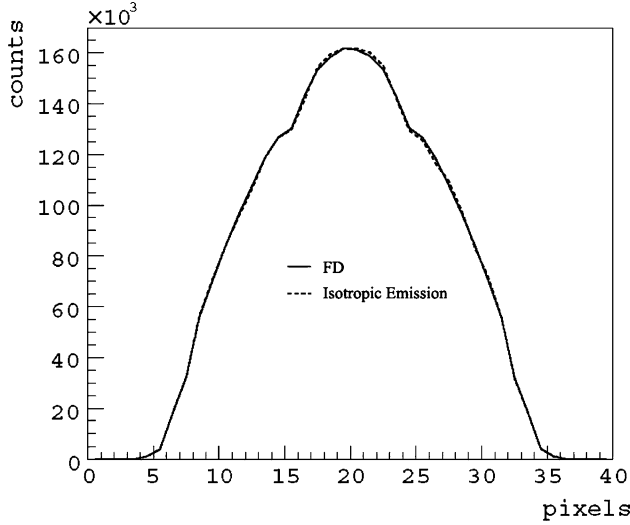


Fig. 7. Profile drawn in the centre of the projection of a cylinder having a radius of 15 mm and a height of 4 mm.

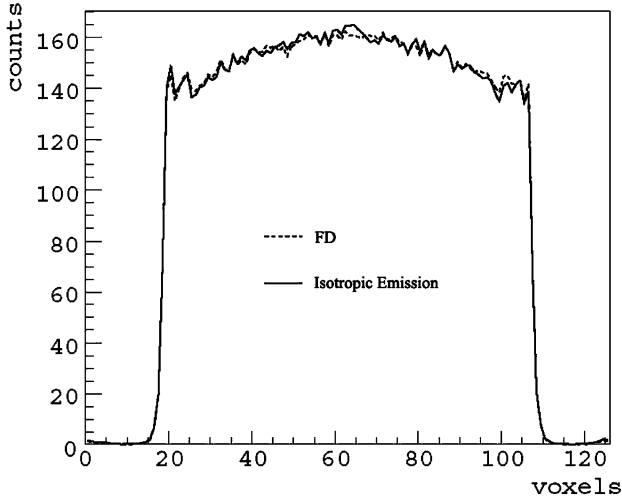


Fig. 8. Profile drawn in an axial slice of the uniform cylinder's images reconstructed from the sinograms calculated respectively using forced detection technique and isotropic emission.

of reconstructed images corresponding to projections calculated with different emission strategies.

### B. Comparison Between FD and KFD

Fig. 9 shows the profiles of the projections obtained at the entrance of the crystal when using the KFD method. Figs. 10 and 11 represent respectively the profiles for both the KFD and the FD method when the interactions within the crystal are modelled using MCS. Profiles are drawn on the fifth and the sixth lines of the projections. Table I shows the time computing and the memory space requirement for both the KFD and the FD method when calculating the PSFs of the considered point source.

### C. Computing Time and Storage Requirement

A total number of  $10^4$  simulations were performed in order to compute the system matrix. For each simulation, 128 projections over  $360^\circ$  were simulated where  $10^6$  photons per pro-

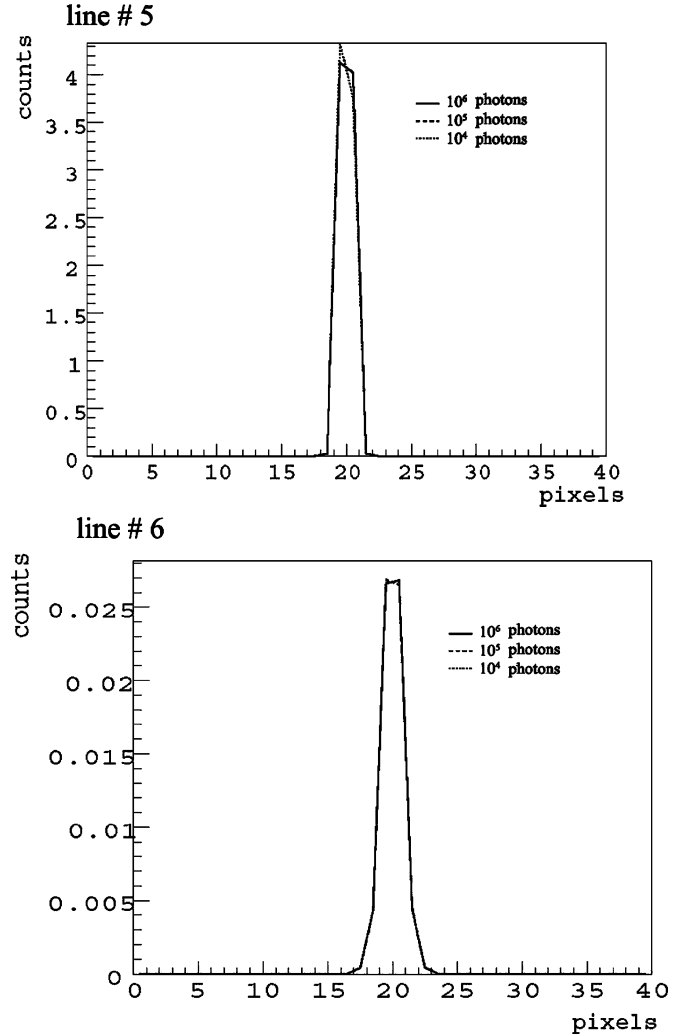


Fig. 9. Profile of the analytic PSF projections at the entry of the crystal for a point source located in the centre of the FOV. Top: line 5. Bottom : line 6.

jection were emitted. The FOV didn't contain any attenuation media and was completely filled with air. Hence, attenuation and scatter occurring in an imaged object or phantom are not taken into account within the elements of the system matrix. The total running time required to perform the totality of the simulations was 120 hours on a grid architecture composed of 128 bi quad-core Xeon L5420. Table II shows the requirement of memory space for matrix storage as function of the dimensions of the voxels and of the clustering choice.

### D. Impact of the Choice of the Considered Number of POI

Fig. 12 shows the projection on the detector of a 1 mm diameter sphere using  $\text{matrix}_9$ ,  $\text{matrix}_{25}$  and  $\text{matrix}_{\text{all}}$ . Two profiles drawn respectively on the fifth and sixth line of the projection are shown in Fig. 13. Fig. 14 shows reconstructed images of an uniform cylinder having a diameter of 30 mm and a height of 4 mm filled with an uniform activity of  $^{99\text{m}}\text{Tc}$ . 128 projections were modelled by Monte Carlo simulation and images were reconstructed with  $\text{matrix}_9$ ,  $\text{matrix}_{25}$  and  $\text{matrix}_{\text{all}}$ . Fig. 15 shows the profiles drawn in an axial slice and a sagittal slice of the reconstructed images.

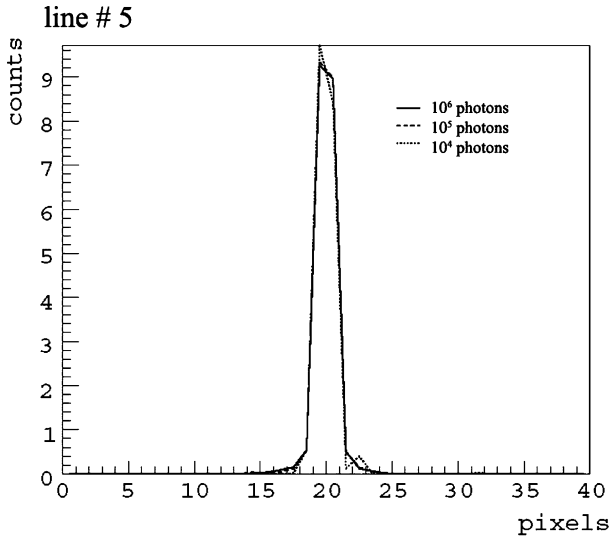


Fig. 10. Profile of the projections for a point source located in the centre of the FOV when using the KFD method. Top: line 5. Bottom : line 6.

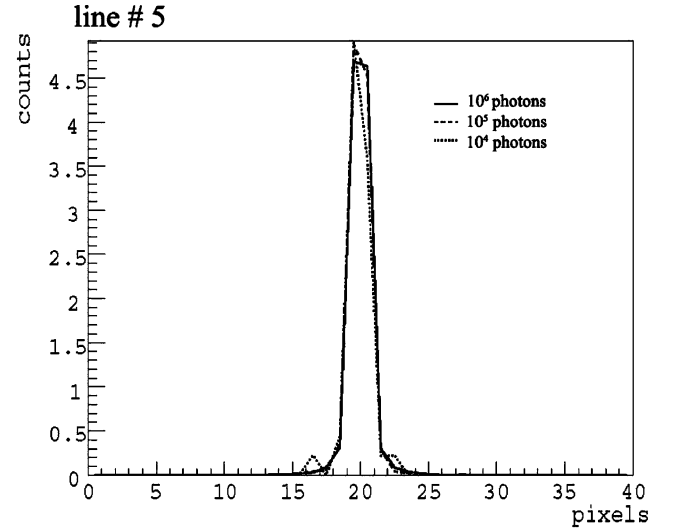


Fig. 11. Profile of the projections for a point source located in the centre of the FOV when using the FD method. Top: line 5. Bottom : line 6.

#### E. Influence of the Number of Photons Used for the System Matrix Calculation on the Reconstructed Images

Improvement in SNR as the number of photons used for the system matrix calculation increases is illustrated in Figs. 16 and 17 respectively for the uniform cylinder and the Jaszczak phantom. Fig. 18 shows the variation of the signal to noise ratio computed in the uniform cylinder images with respect to the number of photons tracks used for the calculation of the system matrix. One can notice that the SNR is clearly improved as the number of photons tracks used of the system matrix calculation increased.

#### F. Quantitative Evaluation

Table III represents the value of the RAR computed for the simulated Jaszczak phantom. RAR values are represented in the cases when using a matrix calculated respectively with  $10^9$  photons histories and  $10^{10}$  photons histories. Values of SNR are also represented for both set of reconstructed images. Fig. 19 shows

TABLE I  
TIME COMPUTING, MEMORY SPACE REQUIREMENT AND NMSE FOR A POINT SOURCE PROJECTION LOCATED IN THE CENTRE OF THE FOV.  $10^6$  PHOTONS WERE USED FOR BOTH FD AND KFD METHOD

Method	Computing Time (s)	Memory space (MBytes)	NMSE
FD	100	13	$2.24 \times 10^{-5}$
KFD	94	150	$4.67 \times 10^{-5}$

TABLE II  
MATRIX SIZE AS FUNCTION OF THE VOXEL DIMENSION

Voxel size (mm <sup>3</sup> )	Full size (GB)	Sparse size (GB)		
		POI 9	POI 25	ALL
0.5×0.5×0.5	21.3	0.79	1.68	3.12
0.33×0.33×0.33	78	2.26	3.82	5.46

the variation of the Restored Activity Ratio (RAR) with respect to the number of iterations between an insert placed at the inner ring and the central insert, and between an insert placed at the

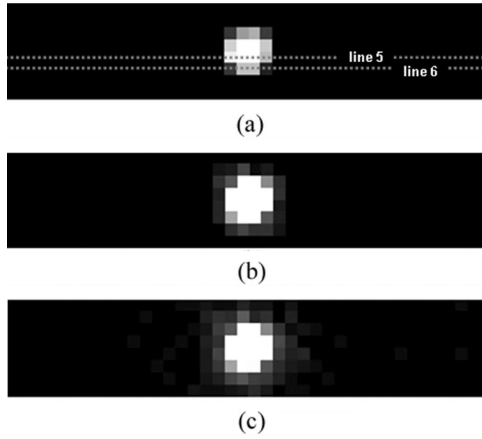


Fig. 12. Projections of a 1 mm diameter sphere positionned in the center of the FOV: (a) 9 POI; (b) 25 POI; (c) ALL pixels are considered while computing projections.

outer ring and the central insert and this for different acquisition time per projection: 1 s, 5 s, 10 s and 15 s.

Fig. 20 shows the reconstruction image of the 13 inserts. Values shown on the figure correspond to the activity ratios between each of the rods and the central one. Ideal values should be equal to one.

#### G. Tomographic Performances

Fig. 21 shows a reconstructed slice of the Derenzo phantom where rods having a diameter of 1 mm are distinguished. The cases where the images were sampled into  $20 \times 84 \times 84$  voxels and  $30 \times 126 \times 126$  voxels are presented.

#### H. Preclinical Studies

Fig. 22 shows fused images from both SPECT and CT modalities. On the coronal slice, the CT images show the trachea where the SPECT images show two hot regions activities located at both sides of the trachea corresponding to the thyroid glands.

### IV. DISCUSSION

In this paper, we first compare two methods enabling the computation of PSFs that take into account the interactions within the crystal in pinhole imaging. While the first method (KFD) models analytically the attenuation within the collimator and then proceed to a detailed MCS of the interactions occuring within the crystal, the second method (FD) models all the detection process using MCS including the interactions in both the collimator and the crystal. We found that both methods model precisely the PSFs.

Figs. 9, 10 and 11 show that noise is mostly due to the interactions in the crystal. Table I shows that when calculating the PSFs using the FD method, less memory space is required to store the output file since less events are detected and hence recorded. The fact that more events are registered using the KFD method can explain why a speed up factor in time computation is not achieved. For this reason, we adopt the FD method in order

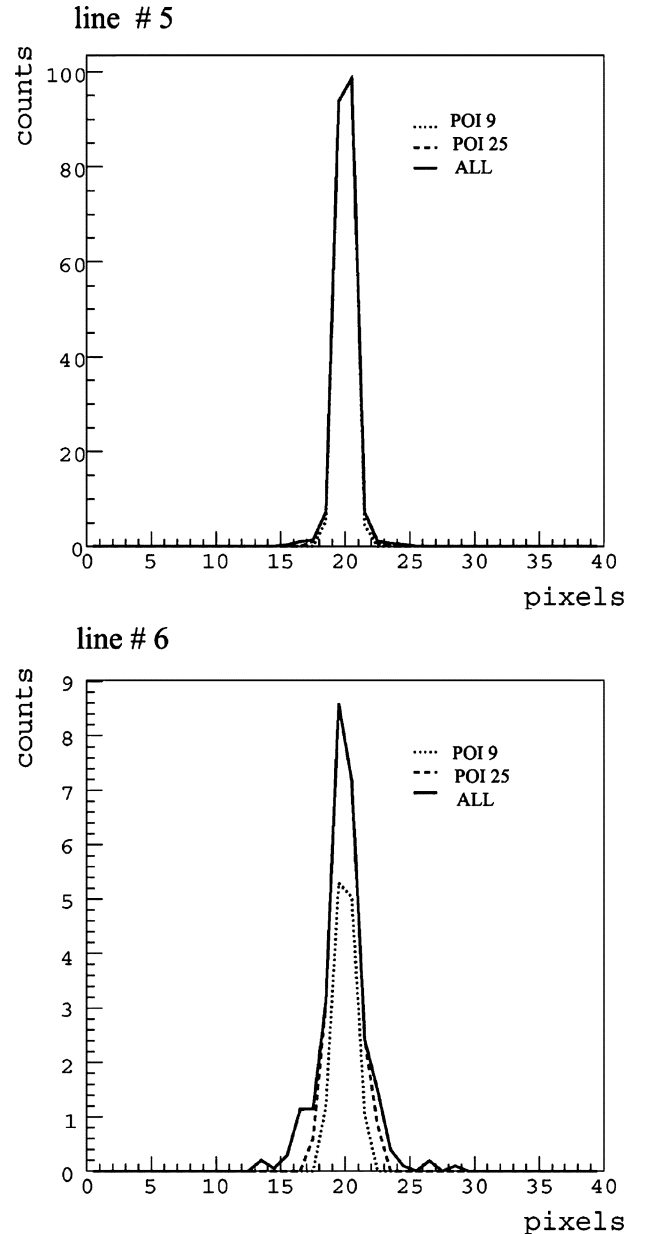


Fig. 13. Representation of a profile drawn on the projection of the point source. Left : Profile drawn on line #5. Right : Profile drawn on line #6.

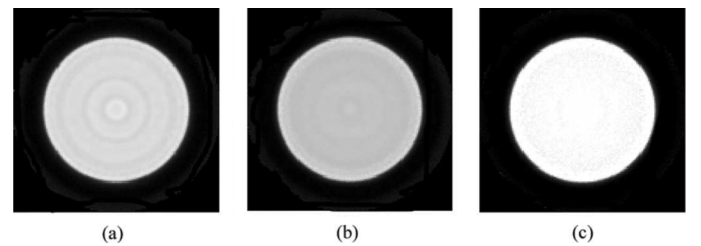


Fig. 14. Reconstructed images of the cylinder using: (a) matrix<sub>9</sub>; (b) matrix<sub>25</sub>; (c) matrix<sub>all</sub>.

to compute the system matrix with a reduced memory space required to store all the raw data necessary for the calculation of the system matrix. The feasibility of the accelerated fully three



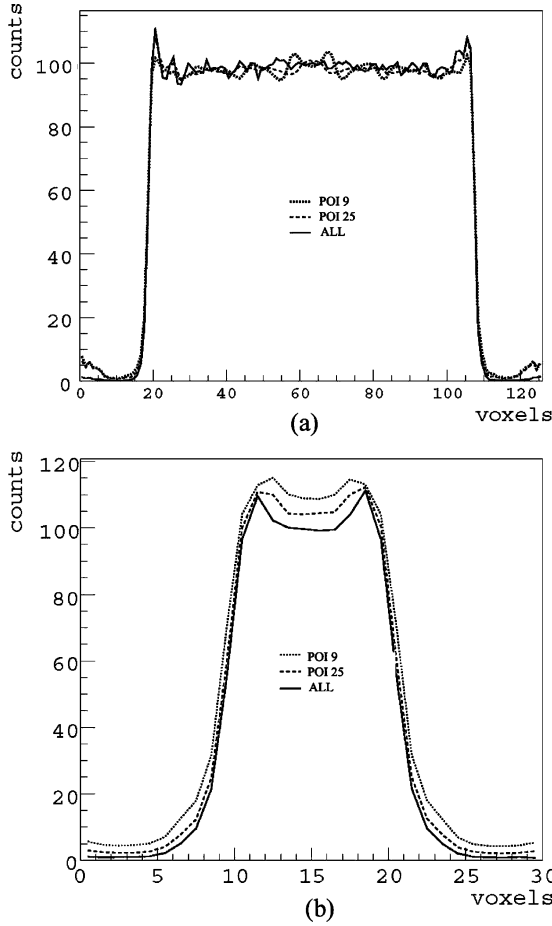


Fig. 15. Profile drawn in the centre slice of reconstructed images of the cylinder using  $\text{matrix}_9$ ,  $\text{matrix}_{25}$  and  $\text{matrix}_{\text{all}}$ . Top: profile drawn in an axial slice. Bottom: profile drawn in a sagittal slice.

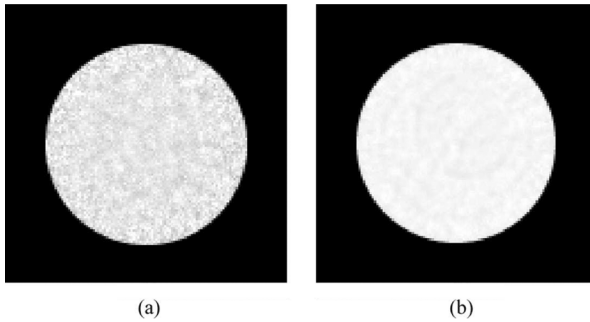


Fig. 16. Reconstructed images of a cylinder (diameter = 30 mm, height = 4 mm) with the ROI within which the SNR is calculated. Reconstruction was done using: (a) matrix calculated with  $10^9$  emitted photons per projection. (b) matrix calculated with  $10^{10}$  emitted photons per projection.

dimensional Monte Carlo reconstruction technique in small animal SPECT has also been validated. The study of the feasibility was done thanks to two techniques enabling the acceleration of Monte Carlo simulations: forced detection technique and parallelizing of Monte Carlo simulations using non-overlapping random number sequences on CG architecture. CG architectures are nowadays accessible to many research teams. The FD technique was first implemented within the Geant4 Monte

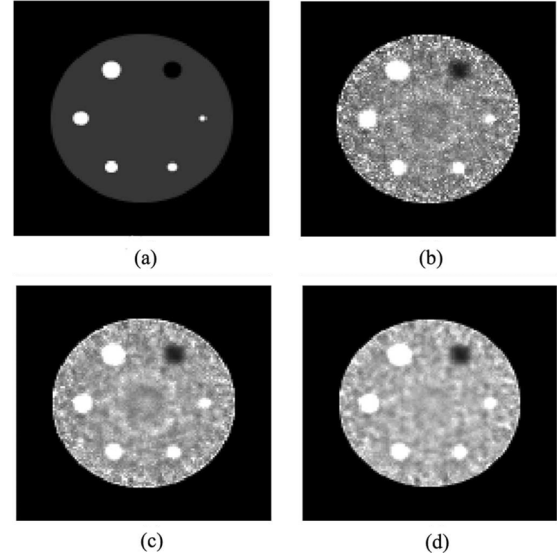


Fig. 17. Images of the reconstructed Jaszczak phantom type: (a) Ideal Image. (b) using matrix calculated with  $10^9$  emitted photons per projection. (c) using matrix calculated with  $5 \times 10^9$  emitted photons per projection. (d) using matrix calculated with  $10^{10}$  emitted photons per projection.

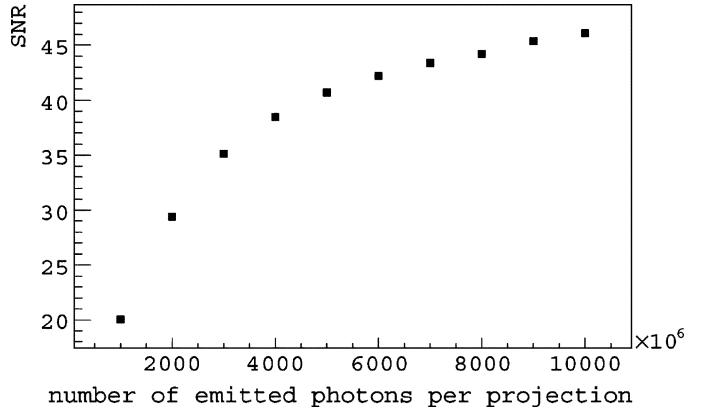


Fig. 18. Signal to noise ratio w.r.t the number of emitted photons per projection for matrix system calculation.

Carlo simulation toolkit. We have shown that the forced detection technique used with an accurate correcting weight factor is similar to the isotropic emission and increases the detection efficiency of the system by a factor of 443 in the considered case.

Table II shows that the memory requirement for the storage of the sparse system matrix is reasonable and makes the management of this latter feasible on an actual single PC. Anyhow, even if system matrix size could become larger due to more photons trajectories simulation, its management can be handled by parallelizing the reconstruction algorithm on a cluster of machines using for example the MPI (Message Passing Interface) language. The computation of the system matrix is time consuming: 120 hours on Computing Grid. However this calculation is done once and for all. The total CPU time needed is estimated to more than 5000 days on a single computer. In addition, the management of a large volume of raw data on a single processor is very difficult. The required time for the system matrix computation can be reduced if Monte Carlo simulations are deployed on more Computing Elements. Furthermore, we can use

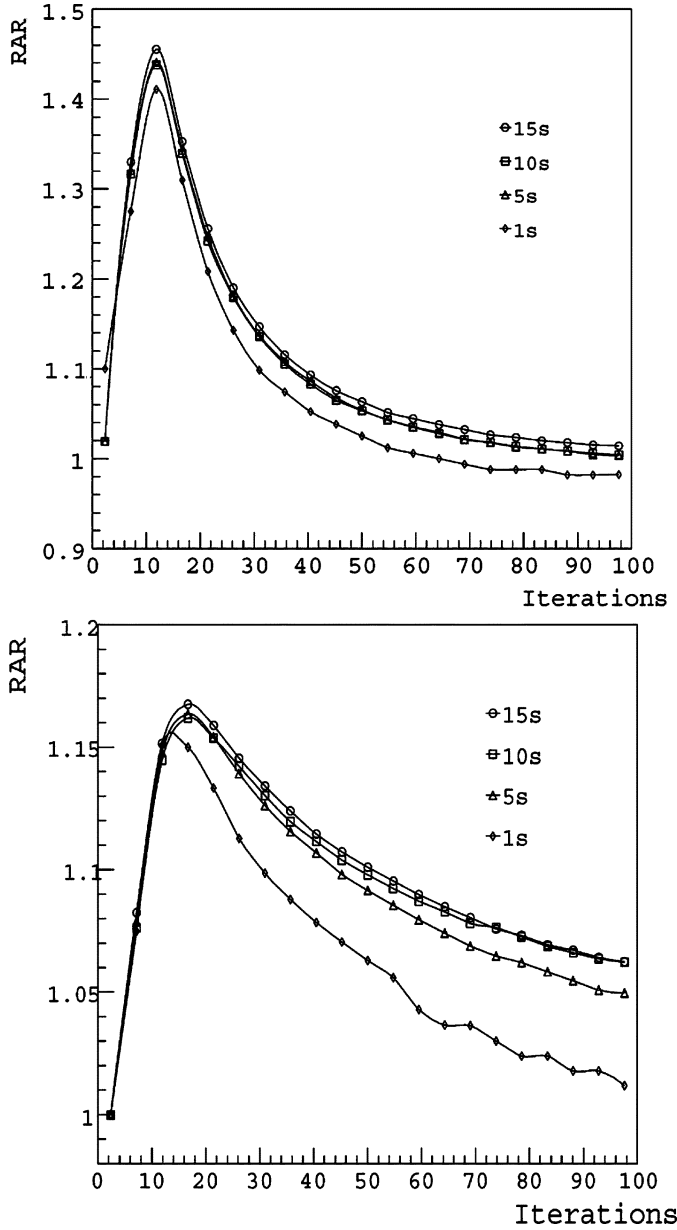


Fig. 19. Variation of the RAR with respect to the number of iterations for different values of number of detected photons within the projections. Top: Values for a rod placed on the outer ring. Bottom: Values for a rod placed on the inner ring.

TABLE III  
RATIO OF ACTIVITY RESTORATION W. R. T THE NUMBER OF EMITTED PHOTONS  
PER PROJECTION FOR MATRIX SYSTEM CALCULATION

Rod #	RAR			
	Ideal	After Sampling	$10^9$ photons	$10^{10}$ photons
Rod 1	5	3.11	$2.38 \pm 1\%$	$2.52 \pm 1\%$
Rod 2	5	3.42	$3.08 \pm 0.9\%$	$3.21 \pm 0.7\%$
Rod 3	5	4.23	$3.51 \pm 0.4\%$	$3.56 \pm 0.4\%$
Rod 4	5	4.11	$3.46 \pm 0.3\%$	$3.54 \pm 0.3\%$
Rod 5	5	3.92	$3.67 \pm 0.3\%$	$3.98 \pm 0.3\%$
Rod 6	0	0.2	$0.31 \pm 2.2\%$	$0.28 \pm 2.4\%$
SNR	-	-	5.68	10.91

axial, coronal and sagittal symmetries in order to reduce the size of the matrix by a factor of eight.

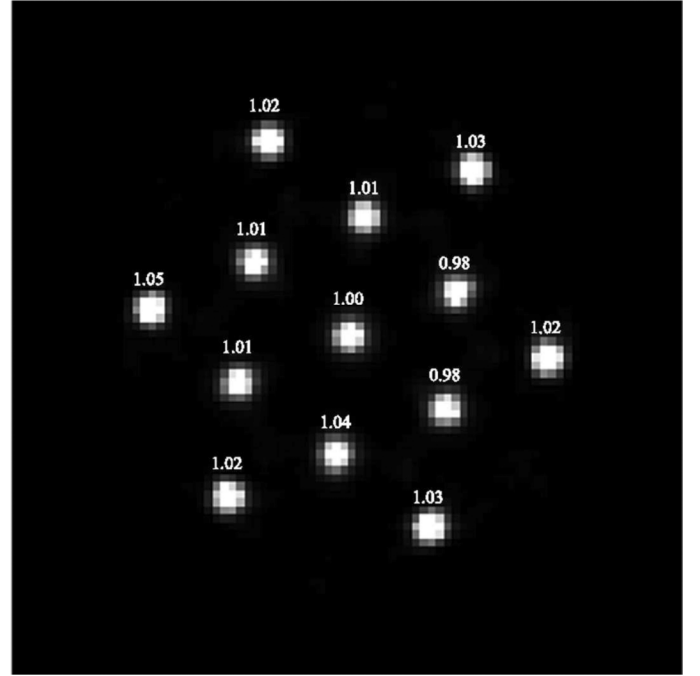


Fig. 20. Slice of the reconstructed image of the phantom composed of 13 rods with RAR value for each of the rods w.r.t the central rod.

The impact of the number of the pixels of interest considered in the computed matrix was studied. It was shown that the projections of a 1 mm diameter sphere are very different whether 9 POI, 25 POI or all pixels were considered. Images reconstructed with  $\text{matrix}_{\text{all}}$  present the best homogeneity and no artifacts unlike the images where  $\text{matrix}_9$ ,  $\text{matrix}_{25}$  were used for reconstruction. Furthermore, reconstructed images are less noisy when the number of POI considered within the system matrix is large (i.e., when scatter of high orders is considered). For this reason, only matrix computed with all the pixels taken into account were used for the reconstruction of the images presented in this paper. This shows the importance of non truncating the PSF function to be integrated in the system matrix in order to avoid artifacts appearance.

We also evaluate the impact of the number of considered photons for the system matrix computing on the signal to noise ratio in reconstructed images. It was found that, as the number of photons considered for the calculation of the system matrix increases, the signal to noise in reconstructed images increases too. The results agreed with the study done in [8] where the decrease of the Mean Square Error as the number of photons increases in the system matrix was shown.

The variation of the Restored Activity Ratios (RAR) as function of the number of iterations and for different acquisition duration per projection (1 s, 5 s, 10 s and 15 s) shows that 5 s acquisition duration is sufficient to perform an accurate relative quantification. The increasing and decreasing bias in the RAR can be explained by the fact that the initial image estimation used in the reconstruction algorithm is a uniform image. During the iterations, the reconstruction algorithm will converge so that hot rods can be distinguished from the background. Values of the RAR seems to be better in short measurements but they have

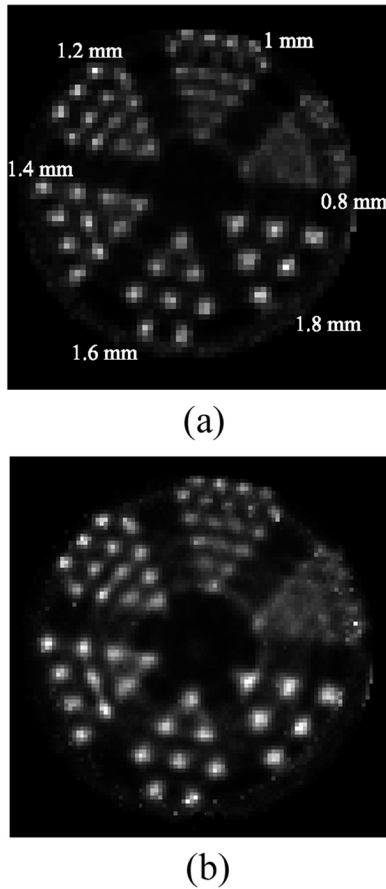


Fig. 21. Reconstructed slice of the Derenzo phantom using MLEM algorithm (100 iterations): (a) voxel dimension =  $0.5 \times 0.5 \times 0.5 \text{ mm}^3$ ; (b) voxel dimension =  $0.33 \times 0.33 \times 0.33 \text{ mm}^3$ .

larger associated deviation. In Fig. 20, we can see that a very good uniformity can be obtained within the field of view.

The tomographic performance study using the Derenzo type phantom shows that a spatial resolution of 1 mm can be achieved using the Accelerated Fully 3D Monte Carlo (AF3DMC) algorithm. Fig. 22 illustrates that the spatial resolution of 1 mm obtained thanks to the modelling of the physical processes occurring within the detector inside the system matrix enables the obtention of a very satisfying reconstructed images of the mouse where the thyroid glands can be distinguished in all of the slices while the salivary glands are observed in axial and sagittal slices.

In this work, the correction for the physical processes occurring within the different phantoms and the animal body are not done. When using the  $^{99\text{m}}\text{Tc}$  (140 keV) as a radiolabeled tracer, the effects of the scatter and the photoelectric absorption within the animal body do not introduce an important bias in the reconstructed images. This is not the case when using the  $^{125}\text{I}$  (27.5 keV) [3]. However, correction for the interactions in the animal body can be done either by integrating the attenuation map obtained by CT exam within MCS for the system matrix computation or by performing an analytic post reconstruction treatment based on the known of the attenuation map. Indeed, integration of the attenuation map in the MSC will increase the computing time comparing to the case where a post reconstruction correction is applied. Comparison of these two correction methods will be the topic of further study.

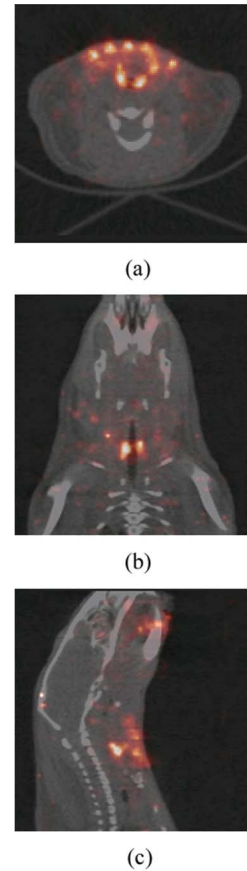


Fig. 22. Reconstructed slices of mouse after injection of pertechnetate: (a) axial slice; (b) coronal slice; (c) sagittal slice.

## V. CONCLUSION

In this paper, we have shown that using a system matrix generated by Monte Carlo Simulations (MCS) for iterative image reconstruction is feasible in a reasonable delay in small animal SPECT thanks to the use of the forced detection technique and the parallelization of MCS on a computing grid architecture.

## ACKNOWLEDGMENT

The authors would like to thank Yannick Patois and Jerome Pansanel for their help in monitoring the computing jobs on the Grid as well as Marc Krauth and Hubert Friedmann for the phantoms that were used for the realistic data acquisition.

## REFERENCES

- [1] D. Lazaro, Z. El Bitar, V. Breton, D. Hill, and I. Buvat, "Fully 3D Monte Carlo reconstruction in SPECT: A feasibility study," *Phys. Med. Biol.*, vol. 50, pp. 3739–3754, 2005.
- [2] Z. El Bitar, D. Lazaro, V. Breton, D. Hill, and I. Buvat, "Fully 3D Monte Carlo image reconstruction in SPECT using functional regions," *Nucl. Instrum. Methods Phys. Res. A*, vol. A569, pp. 399–403, 2006.
- [3] A. C. Sauve, B. W. Reutter, and G. T. Gullberg, "Fully 3D SPECT attenuation and scatter correction using Monte Carlo generated system matrices," in *Proc. 10th Int. Conf. Fully 3D Image Reconstruction in Radiology and Nuclear Medicine*, Beijing, China, 2009, pp. 303–306.
- [4] L. Zhang, S. Staelens, R. Van Holen, and J. De Beenhouwer, "Fast and memory-efficient Monte Carlo-based image reconstruction for whole-body PET," *Med. Phys.*, vol. 37, pp. 3667–3676, 2010.

- [5] M. Rafecas, B. Mosler, M. Dietz, M. Pogl, D. P. McElroy, and S. I. Ziegler, "Use of a Monte-Carlo based probability matrix for 3D iterative reconstruction of MADPET-II data," *IEEE Trans. Nucl. Sci.*, vol. 3, pp. 1775–1779, Jun. 2003.
- [6] S. Shokouhi *et al.*, "Statistical 3D image reconstruction for the RatCAP PET tomograph using a physically accurate Monte Carlo based system matrix," in *Proc. IEEE Nuclear Science Symp. Conf. Rec.*, 2004, vol. 6, pp. 3901–3905.
- [7] L. A. Shepp and Y. Vardi, "Maximum likelihood reconstruction for emission tomography," *IEEE Trans. Med. Imag.*, vol. 1, pp. 113–122, 1982.
- [8] J. Qi and R. Huesman, "Effect of errors in the system matrix on maximum *a posteriori* image reconstruction," *Phys. Med. Biol.*, vol. 50, pp. 3297–3312, 2005.
- [9] J. W. Beck, R. J. Jaszcak, R. E. Coleman, C. F. Sterner, and P. Nolte, "Analysis of SPECT including scatter and attenuation using sophisticated Monte Carlo modeling methods," *IEEE Trans. Nucl. Sci.*, vol. NS-29, no. 1, pp. 506–511, Feb. 1982.
- [10] M. Ljungberg and S. E. Strand, "Attenuation and scatter correction in SPECT for sources in a nonhomogeneous object: A Monte Carlo study," *J. Nucl. Med.*, vol. 32, pp. 1278–1284, 1991.
- [11] H. Wang, R. J. Jaszcak, and R. E. Coleman, "Monte Carlo modeling of penetration effect for iodine-131 pinhole imaging," *IEEE Trans. Nucl. Sci.*, vol. 435, no. 6, pp. 3272–3277, Dec. 1996.
- [12] H. Wang, R. J. Jaszcak, D. R. Gilland, K. L. Greer, and R. E. Coleman, "Solid geometry based modeling of nonuniform attenuation and Compton scattering in objects for SPECT imaging systems," *IEEE Trans. Nucl. Sci.*, vol. 40, no. 4, pp. 1305–1312, Aug. 1993.
- [13] M. Gieles, H. W. A. M. de Jong, and F. J. Beekman, "Monte Carlo simulations of pinhole imaging accelerated by kernel-based forced detection," *Phys. Med. Biol.*, vol. 47, pp. 1853–1867, 2002.
- [14] H. W. A. M. de Jong, E. T. P. Slijpen, and F. J. Beekman, "Acceleration of Monte Carlo SPECT simulations using convolution-based forced detection," *IEEE Trans. Nucl. Sci.*, vol. 48, no. 1, pp. 58–64, Feb. 2001.
- [15] J. De Beenhouwer, S. Staelens, S. Vandenberghe, and I. Lemahieu, "Acceleration of GATE SPECT simulations," *Med. Phys.*, vol. 35, no. 4, pp. 1476–1485, 2008.
- [16] H. W. A. M. de Jong, W. T. Wang, E. C. Frey, M. A. Viergever, and F. J. Beekman, "Efficient simulation of SPECT down-scatter including photon interactions with crystal and lead," *Med. Phys.*, vol. 29, no. 4, pp. 550–560, 2002.
- [17] R. Reuillon, D. Hill, Z. El Bitar, and V. Breton, "Rigorous distribution of stochastic simulations using the DistMe toolkit," *IEEE Trans. Nucl. Sci.*, vol. 55, no. 1, pp. 595–603, Feb. 2008.
- [18] L. Maigne *et al.*, "Parallelization of Monte Carlo simulations and submission to a grid environment," *Parallel Process. Lett.*, vol. 14, pp. 177–196, 2004.
- [19] Z. El Bitar, B. Leh, V. Bekaert, D. Huss, and D. Brasse, "Performances' evaluation of a pinhole small animal SPECT system," in *Proc. IEEE Nuclear Science Symp. and Medical Imaging Conf.*, 2008, pp. 3801–3804.
- [20] M. F. Smith and R. J. Jaszcak, "An analytic model of pinhole aperture penetration for 3D pinhole SPECT image reconstruction," *Phys. Med. Biol.*, vol. 43, pp. 761–775, 1998.
- [21] S. D. Metzler, J. E. Bowsher, M. F. Smith, and R. J. Jaszcak, "Analytic determination of pinhole collimator sensitivity with penetration," *IEEE Trans. Med. Imag.*, vol. 20, pp. 730–741, Aug. 2001.
- [22] S. Agostinelli *et al.*, "GEANT4—A simulation toolkit," *Nucl. Instrum. Methods Phys. Res. A*, vol. A506, pp. 250–303, 2003.
- [23] M. Matsumoto and T. Nishimura, "Mersenne Twister: A 623-dimensionally equidistributed uniform pseudorandom number generator," in *Proc. 29th Conf. Winter Simulation*, 1997, pp. 127–34.
- [24] S. Jan *et al.*, "GATE, a simulation toolkit for PET and SPECT," *Phys. Med. Biol.*, vol. 49, no. 19, pp. 4543–4561, 2004.